Dynamics and fluctuations of minimally structured glass formers

Patrick Charbonneau [1,2] Yi Hu [1,*] and Peter K. Morse [1,3,4,5]
[1]*Department of Chemistry, Duke University, Durham, North Carolina 27708, USA*
[2]*Department of Physics, Duke University, Durham, North Carolina 27708, USA*
[3]*Department of Chemistry, Princeton University, Princeton, New Jersey 08544, USA*
[4]*Department of Physics, Princeton University, Princeton, New Jersey 08544, USA*
[5]*Princeton Institute of Materials, Princeton University, Princeton, New Jersey 08544, USA*

(Received 2 January 2024; accepted 22 April 2024; published 23 May 2024)

The mean-field theory (MFT) of simple structural glasses, which is exact in the limit of infinite spatial dimensions, $d \to \infty$, offers theoretical insight as well as quantitative predictions about certain features of $d = 3$ systems. In order to more systematically relate the behavior of physical systems to MFT, however, various finite-d effects need to be accounted for. Although some efforts along this direction have already been undertaken, theoretical and technical challenges hinder progress. A general approach to sidestep many of these difficulties consists of simulating minimally structured models whose behavior smoothly converges to that described by the MFT as d increases, so as to permit a controlled dimensional extrapolation. Using this approach, we here extract the small fluctuations around the dynamical MFT captured by a standard liquid-state observable, the non-Gaussian parameter α_2. The results provide insight into the physical origin of these fluctuations as well as a quantitative reference with which to compare observations for more realistic glass formers.

DOI: 10.1103/PhysRevE.109.054905

I. INTRODUCTION

Solving the dynamics of structural glass formers remains a frontier problem in statistical physics. Even hard spheres, one of the simplest such model, present nontrivial physics in the densely supercooled regime that cannot be described by conventional kinetic theory or hydrodynamics. The mode-coupling theory of glasses (MCT), first developed in the 1980s, provides a microscopic description that does accurately describe certain aspects of the dynamical slowdown upon supercooling a liquid [1]. That theoretical description, however, lacks a straightforward limit in which it becomes exact that could be used to systematically study deviations from its predictions in physical systems.

Over the past 15 years, an altogether different approach, the mean-field theory (MFT) of simple structural glasses—hard-sphere-like and related systems—has been steadily worked out [2–4]. While the MCT equations were obtained from uncontrolled approximations, the MFT approach is exact in the specific limit—albeit far from physical reality—of an infinite number of spatial dimensions, $d \to \infty$. Being solvable numerically, it captures certain aspects of finite-d jamming physics with remarkable accuracy and predicts a novel type of (Gardner) transition in amorphous solids that has found various experimental echoes [5–8]. From a theoretical physics standpoint, it has also brought descriptions that were based on loose physical analogies with spin glasses under a single coherent umbrella. For instance, it has confirmed the validity of the random first-order transition (and associated scenarios) in the limit $d \to \infty$ as well as the mean-field–like structure of the MCT equations, despite their quantitative failings [9,10].

The MFT of simple structural glasses, however, is no panacea either. By construction, it neglects fluctuations and only accounts for minimal pairwise correlations. (Including higher-body correlations, which vanish as $d \to \infty$, would require an even richer—and more unwieldy—cluster-based approach [11].) These simplifications obfuscate the possible connection between MFT and the structurally and dynamically rich behavior of $d = 3$ glass formers. Early efforts to estimate the impact of finite-dimensional pair structure correlations on the MFT-like caging transition have been met with only limited success [12,13]. More recently, the extent and nature of small caging fluctuations have been more successfully considered [14,15]. Large (instantonic) deviations, however, remain out of reach even for single-particle processes [16].

The dynamical MFT (DMFT) [17,18], which notably provides equations that describe the time evolution of the mean squared displacement (MSD), $\Delta(t)$, also remains challenging to hammer out. Its analytical formulation is so complex that only under a limited range of conditions can it be evaluated at this time [19,20]. Out-of-equilibrium conditions are particularly thorny [21–24]. To tease out some of the out-of-equilibrium physics, recent efforts have focused on simulating minimally structured models of glasses in finite d and extrapolating the results to the limit $d \to \infty$ [20,25]. An advantage of these abstract models is that certain aspects of their physics are by construction closer to the mean-field predictions. In that sense, that approach is akin to using the Gaussian-core model as a reference for the standard Kob-Anderson glass model in three dimensions [26]. In both cases, the reference model exhibits stronger mean-field physics and therefore more quantitatively matches the theoretical predictions. Only in the former, however, is the relationship formally justified,

*yi.hu@duke.edu

thus allowing more systematic studies to be conducted and stronger conclusions to be reached.

Although computing small dynamical fluctuations around the equilibrium DMFT also remains out of theoretical reach, a first-principle understanding of the origin of single-particle contributions was recently worked out in Ref. [14]. That work introduced the (single-particle) dynamical susceptibility $\chi_4(t)$, defined as the variance of particle displacements, thus naturally capturing the fluctuations of the MFT/DMFT natural order parameter, $\Delta(t)$. The quantity is physically analogous to other four-point susceptibilities previously defined, which typically rely on density correlations [27,28], but its formulation is a bit more versatile. The observable, which naturally describes small fluctuations in the caging regime, can indeed be linearly related with the non-Gaussian parameter $\alpha_2(t)$. The observable was first introduced by Rahman [29] in the early days of molecular simulation, and then commonly used to assess the dynamical heterogeneity of supercooled liquids [30–32], including in MCT [33,34]. (A full consideration of MCT predictions for this quantity is left as future work [35].) From a theoretical physics lens, the DMFT describes the single-particle equilibrium dynamics as a Langevin equation with a purely Gaussian (albeit colored) noise, which can be integrated to obtain $\Delta(t)$ [17,18]. Given that the description is exact when $d \to \infty$, deviations of the self–van Hove function from Gaussianity are therefore necessarily finite-d corrections. In order to determine if $d = 3$ observations of $\alpha_2(t)$ in simple structural glass formers in any way reflect fluctuations around the DMFT, however, these fluctuations first ought to be somehow quantified.

Here, building on the approach developed to study the out-of-equilibrium DMFT, we extract the $d \to \infty$ behavior of $\alpha_2(t)$ by studying and comparing two minimally structured models, the random Lorentz gas (RLG) and the Mari-Kurchan (MK) model (see Sec. II for definitions), that separately converge to the MFT of simple structural glasses in the high d limit [16,36]. Finite d versions of these models can therefore be viewed as exhibiting perturbative deviations relative to the exact $d \to \infty$ solution. In other words, these deviations—at least noninstantonic ones—then scale in $1/d$ and can be reasonably controlled through dimensional extrapolation. In passing, we validate the DMFT description of the MSD in the limit $d \to \infty$ as well as the associated small caging fluctuations. The plan for the rest of this article is as follows. Section II describes the models considered and the simulation approach and Sec. III presents and discusses the numerical results. A brief conclusion follows in Sec. IV.

II. MODELS AND SIMULATION METHODS

The RLG is a point tracer that evolves within the void (empty) space left by Poisson distributed spherical obstacles of unit radius and scaled density $\hat{\varphi} = \rho V_d/d$, where ρ and V_d denote the point intensity (number density) and the d-dimensional unit radius sphere volume, respectively. It is here simulated as in Refs. [14,16,37]. Initial configurations are obtained using a cavity reconstruction scheme [14,16]. In the caging regime, for densities above the MFT dynamical transition at which glasslike (and MCT-like) caging emerges, $\hat{\varphi} \gtrsim \hat{\varphi}_\mathrm{d}$, the tracer is placed at the origin and surrounded by a spherical shell of obstacles that precludes overlaps with the tracer and is of sufficient thickness to prevent its escape over the simulation time. Each realization thus defines a cage, whose size is defined as the long-time value of the MSD plateau of a given tracer. In the diffusive regime, for $\hat{\varphi} \lesssim \hat{\varphi}_\mathrm{d}$, initial configurations are obtained through quiet planting [16,38]. This approach is implemented by placing the tracer at the center of a simulation box and then distributing obstacle positions uniformly at random within that box, rejecting any obstacles that cover the origin. A typical simulation box consists of 10^5 obstacles for $d = 3$ and up to 10^6 obstacles for $d = 24$. Results are averaged over at least 10^3 independent realizations of obstacle positions.

The Mari-Kurchan (MK) model [39,40] consists of N hard spherical particles of unit diameter interacting through shifted pair interactions. It is simulated as in Ref. [36]. Here again, initial configurations are obtained by quiet planting [36]. After placing particles uniformly at random within the simulation box, pairwise shifts are sampled uniformly at random within that box, but values that result in the pair overlapping are rejected. Like for the RLG, a scaled density can be defined $\hat{\varphi} = 2^d \rho V_d/d$, where the factor of 2^d accounts for the different obstacle diameter conventions used in the two models. Again, in the caging regime $\hat{\varphi} \gtrsim \hat{\varphi}_\mathrm{d}$, most particles are dynamically trapped by the surrounding particles (except those experiencing hopping events [36]). The long-time value of the MSD plateau of each caged particle is then used to define the cage size.

A. Mapping between two models

As described in Refs. [16,20,41], in the $d \to \infty$ limit, the two models only differ by a trivial scaling factor,

$$\begin{aligned} 2\hat{\varphi}_\mathrm{RLG} &\leftrightarrow \hat{\varphi}_\mathrm{MK}, \\ \hat{\Delta}_\mathrm{RLG} &\leftrightarrow 2\hat{\Delta}_\mathrm{MK}, \\ [\langle \hat{r}^4(t)\rangle]_\mathrm{RLG} &\leftrightarrow 4[\langle \hat{r}^4(t)\rangle]_\mathrm{MK}, \end{aligned} \tag{1}$$

where $\hat{\Delta}(t) = d\Delta(t)$ for the MSD $\Delta(t) = [\langle r^2(t)\rangle]$ and $[\langle \hat{r}^4(t)\rangle] = d^2[\langle r^4(t)\rangle]$ for the mean quartic displacement, after thermal $\langle \ldots \rangle$ averaging (over displacements within a cage) and disorder $[\ldots]$ averaging (over cage realizations). For notational convenience, in the rest of the text we omit the subscript (RLG or MK) when the discussion applies to both models or when the model is clearly specified in the surrounding text.

By contrast, no universal mapping is possible for the dynamical susceptibility $\chi_4(t) = [\langle r^4(t)\rangle] - \Delta^2(t)$ (and the scaled $\hat{\chi}_4 = d([\langle \hat{r}^4(t)\rangle] - \hat{\Delta}^2) = d^3\chi_4$ [14]). The two models are nevertheless expected to correspond in certain limits (see Appendix A),

$$\hat{\chi}_\mathrm{4,RLG} \leftrightarrow \begin{cases} 4\hat{\chi}_\mathrm{4,MK}, & \text{short times and long-time diffusion,} \\ 8\hat{\chi}_\mathrm{4,MK}, & \text{long-time caging.} \end{cases} \tag{2}$$

Finally, the mean tracer velocity, which controls the scaling of time of the RLG, can be chosen arbitrarily. For convenience, the scaled time for the RLG is here aligned with that of the MK model (and with the reference DMFT calculation),

$$\hat{t}_\mathrm{RLG} \leftrightarrow \hat{t}_\mathrm{MK}. \tag{3}$$

When the tracer mean velocity is set to unity, this choice leads to $\hat{t} = \sqrt{d}t$ and $dt/2$ for the Newtonian and Brownian RLG, respectively, and $\sqrt{2}dt$ for the Newtonian MK model.

B. Simulation boxes

Simulations are generally run in boxes under checkerboard D_d periodic boundary conditions, as described in Refs. [13,37]. This setup enables a system size reduction of a factor of $2^{(d-2)/2}$ relative to standard (hyper)cubic boundary conditions Z_d for similar finite-size corrections from the thermodynamic limit. For the MK model, in which the number of pairs of coordinate shifts, $\mathcal{O}(N^2)$, sets the memory complexity, simulations up to $d = 8$ are then numerically accessible. The chosen system size aims to balance computational cost and finite-size corrections, such that the MSD is not affected significantly ($\lesssim$1% systematic error). We here find that $N = 3000$ suffices for all cases except for $\hat{\varphi} > \hat{\varphi}_\mathrm{d}$ in $d = 8$. For instance, $N = 10\,000$ is needed for $\hat{\varphi} = 20$, thus limiting the computationally accessible range of densities.

The single-particle nature of the RLG model allows for the dimensional range to stretch to $d = 12$ under similar conditions. That range, however, can be further expanded by using periodic boundary conditions with the $d = 24$ Leech lattice symmetry, Λ_{24} [42,43]. This exceptionally dense arrangement allows for a reduction in system size by up to a factor of 2^{24} and 2^{13} relative to a system under periodic boundary conditions of Z_{24} (hypercubic) and D_{24} symmetry, respectively [13]. Despite this remarkable efficiency gain, we argued in Ref. [13] that the decoding cost of Λ_{24} was nevertheless too onerous to make it computationally practical. A more efficient decoder devised by Vardy *et al.* [44] has since come to our attention. In contrast to the original algorithm by Conway *et al.* [42], it follows from a maximum likelihood decoding approach, which requires only 3595 operations (versus 55 968 for that of Ref. [42]) to identify the minimal image of a particle. This improvement makes the approach computationally tractable at this time. In this work we use an open-source integer implementation of this algorithm [45] as reference library and straightforwardly extend it to floating point coordinates.

The resulting implementation provides roughly 1.2×10^5 queries-per-second (QPS) performance for the minimal image computation (tested on Intel Xeon E5-2680 v3 CPU single core). It then takes four hours to run a $d = 24$ system with $N = 10^6$ up to $\hat{t} = 10^5$. For reference, running the MK model in $d = 8$ with $N = 3000$ up to $\hat{t} = 10^5$ takes three days on that same architecture.

C. Microscopic dynamics

A standard event-driven implementation of Newtonian dynamics is used for both the RLG and the MK model [36,46]. For the RLG, however, a subtle correction also needs to be taken into account. Earlier numerical simulations used a unit tracer velocity throughout [14,16,37]. For a one-particle system, this microcanonical ensemble setup does not recover the (Gaussian) Maxwell-Boltzmann distribution of velocities that is expected for an equilibrium multiparticle system. As a result, the self–van Hove function is then non-Gaussian at short times [14]. Although such microscopic details of the dynamics are expected to be irrelevant at long times upon approaching $\hat{\varphi}_\mathrm{d}$ and beyond, the resulting short-time deviations are sufficiently significant to partly obfuscate the emergence of interesting features at intermediate times. In order to sidestep this difficulty, we here assign the tracer an initial velocity taken from a Gaussian distribution, so as to recover the Maxwell-Boltzmann distribution of velocities. The tracer velocity (preserving its direction) is also reassigned with probability $p = 1/d$ at each collision. Because the tracer collision rate (number of collisions per unit time) scales as $\hat{Z}_\mathrm{tracer} \sim d\hat{\varphi}$ (see Appendix B), this choice results in a d-independent scaling of the decorrelation time from the initial velocity rate that matches that of multiparticle models, such as standard and MK hard spheres. The long-time dynamics of the system remains unaffected.

For the RLG, Brownian dynamics is also considered, using de Michele's event-driven scheme [47,48]. In this scheme, at the end of every time interval $\Delta\hat{t}_n = 2^n\Delta\hat{t}_0 \leqslant 1/2$ particle velocity is reset to a multivariate Gaussian random variable, $\boldsymbol{v} = \boldsymbol{g}/\sqrt{\Delta\hat{t}_n}$. As minimal time interval, we choose $\Delta\hat{t}_0 = \hat{t}_\mathrm{min}/10$, where $\hat{t}_\mathrm{min}$ is the smallest sampling time interval of correlations; after sampling $\hat{t}_\mathrm{min}$ for 2^{10} times (at $\hat{t} = 2^{10}\hat{t}_\mathrm{min}$), we set $n = 1$, after sampling $2\hat{t}_\mathrm{min}$ for 2^{10} times (at $\hat{t} = 2^{11}\hat{t}_\mathrm{min}$), we set $n = 2$, and so on until $\Delta\hat{t}_n \leqslant 1/2$. This strategy recovers the Brownian statistics at short times, while avoiding the excessive computational cost of repeatedly regenerating random velocities and recalculating subsequent collisions over longer timescales, where this effect plays no notable role.

III. RESULTS AND DISCUSSION

Using the RLG and MK model simulation results, Sec. III A compares the time evolution of the MSD in finite d with the exact $d \to \infty$ DMFT results from Ref. [19] and Sec. III B considers the long-time behavior of the MSD. Finite-d fluctuations in those two regimes are then examined in Secs. III C and III D, respectively.

A. MSD time evolution

In order to validate the perturbative nature of these models, the MSD from numerical simulations is first compared with the DMFT prediction of Ref. [19] for $d \to \infty$ hard spheres. Results for the MK model are expected to naturally converge to that limit as d increases and those for the RLG to do so after Eq. (1) rescaling. For the RLG, an additional effect must be taken into account. As carefully discussed in Ref. [16], for $d \lesssim 8$ the percolation transition ($\hat{\varphi}_\mathrm{p}$) takes place at densities for which MFT predicts that the tracer should diffuse [16]. Because percolation physics is not perturbative relative to the MFT of simple structural glasses, results in its vicinity do not smoothly converge to the DMFT prediction [see, e.g., $\hat{\varphi} = 2$ lines at long times for $d = 3, 6$ in Fig 1(b)]. Therefore, for $\hat{\varphi}_\mathrm{p} < \hat{\varphi} < \hat{\varphi}_\mathrm{d}$, we only consider the short-time MSD, i.e., for $\hat{t} \ll D^{-1}$, where D is the diffusivity constant.

Once these effects are accounted for, the dimensional evolution of the MSD is smooth for both the RLG and the MK model (Fig. 1). For systems with Newtonian dynamics, the trend is robust down to $d = 3$. Low and high density results exhibit only small deviations from the DMFT predictions.

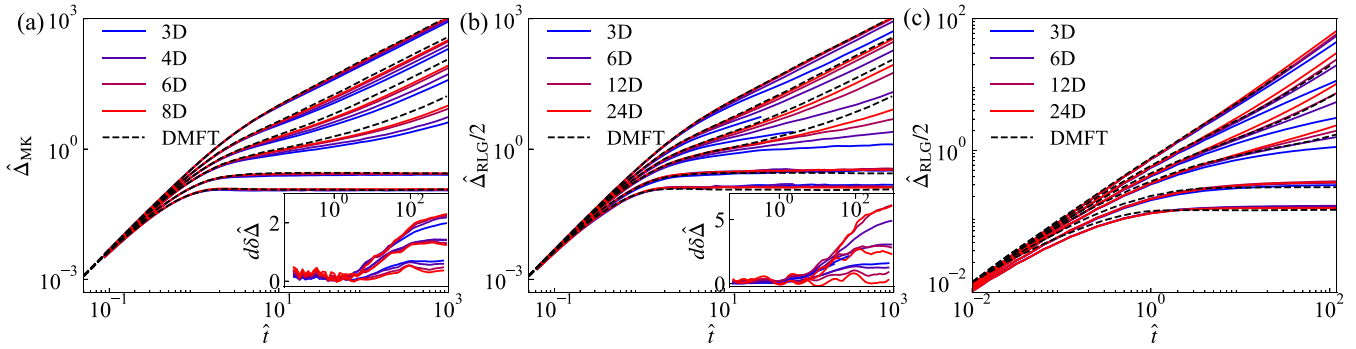

FIG. 1. MSD for (a) the MK model at $\hat{\varphi} = 1, 2, 3, 4, 6, 8$ (from top to bottom) with Newtonian dynamics and for the RLG at corresponding $\hat{\varphi} = 0.5, 1, 1.5, 2, 3, 4$ (from top to bottom) with (b) Newtonian and (c) Brownian dynamics. Numerical solution of the DMFT equations are also included (dashed black lines) [19]. (Insets) Rescaled deviation of simulation results from the DMFT prediction for Newtonian dynamics with (a) $\hat{\varphi} = 1, 2, 3$ and (b) $\hat{\varphi} = 0.5$, 1, and 1.5 (from bottom to top). Insets have the same x axis as the main panels. In all cases, a scaling collapse is achieved as d increases, but the correction is smaller for the MK model than for the RLG at corresponding densities. DMFT predictions for Brownian dynamics deviate too strongly from finite-d results for a similar collapse to be attempted.

As expected from studies of caging susceptibility [14,15], significantly larger deviations emerge upon approaching $\hat{\varphi}_d$. In all cases, deviations from the exact $d \to \infty$ MFT results are consistently perturbative as (Fig. 1 insets)

$$\delta\hat{\Delta}(\hat{t}) = \frac{|\hat{\Delta}_{MFT}(\hat{t}) - \hat{\Delta}(d,\hat{t})|}{\hat{\Delta}_{MFT}(\hat{t})} \sim 1/d. \tag{4}$$

For $\hat{\varphi} \ll \hat{\varphi}_d$, the collapse is nearly quantitative, but higher-order deviations can be detected for $d = 3$ at the highest (diffusive) density considered. In all cases, the overall perturbation is about twice as large for the RLG than for the MK model.

By contrast, Brownian dynamics simulations deviate from DMFT predictions at all times. They are overestimated at short times, $\hat{t} \lesssim 1$, and underestimated at long times, $\hat{t} \gtrsim 10^1$. For the former, the analytical expansion of the MSD reveals that the associated discrepancy follows from numerical imprecision in solving the DMFT equations [19] (see Appendix C). For the latter, Ref. [19] noted already that although the equations are exact in the $d \to \infty$ limit, a singularity in the memory function gives rise to severe numerical integration challenges. In the caging regime, this difficulty was found to result in the long-time limit of the MSD from the DMFT differing from the (independent) static MFT analysis [19]. Although no similarly systematic comparison can be made in the diffusive regime, one can reasonably expect the same underlying issue to be at play there as well.

B. MSD long-time scaling

As a further validation of the perturbative nature of these models in finite d, we consider the long-time MSD in the caging regime (Fig. 2 and [41], Fig. 3). Here again, a smooth dimensional evolution is observed. An interesting difference between the finite-d RLG and MK model is nevertheless noted. While both systems have $\hat{\Delta}(d,\hat{t}) < \hat{\Delta}_{MFT}(\hat{t})$ in the diffusive regime, deviations are of opposite sign in the caging regime. A previous work by some of us [41] introduced the modal squared displacement in addition to the conventional mean squared displacement. Interestingly, the sign of the deviation was found to differ between the mean and the modal squared displacements of the RLG, as a result of a heavy tail in the probability distribution of cage sizes in that system. The absence of such a distinction in the MK model suggests a significantly smaller cage size anisotropy. To quantify this effect more carefully, we repeat for the MK model the RLG analysis in Ref. [41] for the long-time plateau [$\hat{\Delta} = \hat{\Delta}(\hat{t} \to \infty)$] of both mean and modal cage sizes (Fig. 2). We also follow Ref. [14], Fig. 2(b) in fitting the cage sizes distribution with a log-normal form, which describes the distribution well even for $d = 3$. By contrast, the large tail observed in the RLG model at corresponding d and $\hat{\varphi}$ markedly deviates from a log-normal form. In other words, cages for the MK model are more narrowly distributed than for the RLG [see Eq. (2)] and seemingly less affected than the RLG by nonperturbative (instantonic) hopping effects [16,36].

As expected from an earlier report [36], the cage size—as determined from both the modal and the mean squared displacements—closely follows the MFT prediction for all d considered nearly down to $\hat{\varphi}_d$. Its predicted square-root singularity at $\hat{\varphi}_d$, however, is expected to be rounded by hopping in finite d [36]. Here again, these processes are less prevalent in the MK model than in the RLG. For instance, for $\hat{\varphi} = 5.5$, $\hat{\Delta}(\hat{t} = 10^4)/\hat{\Delta}(\hat{t} = 10^2) = 1.002$, which results in a difference in $d\delta\hat{\Delta}$ of only about 1%, while for the RLG a comparable convergence is only possible for $2\hat{\varphi}_{RLG} \geqslant 6$ [41]. A "long-time" plateau can therefore be identified in the MK model at lower $\hat{\varphi}$ without resorting to the modal displacement to screen away the fat tail of large displacements. From this standpoint, finite d cages in the MK model are clearly better defined than in the RLG.

A consideration of the perturbative regime more specifically finds that although higher-order deviations from $d \to \infty$ results are noticeable in $d = 3$ and 4, the $1/d$ collapse appears converged by $d = 6$–8 at high $\hat{\varphi}$ (Fig. 2 insets), which is also consistent with fluctuations being relatively small in this model. Although the perturbative prefactor grows upon approaching $\hat{\varphi}_d$ in a way consistent with a divergence, the available d range is insufficient to probe that phenomenon directly. Results for $\hat{\varphi} = 5$ indeed already deviate from the expected scaling in the higher d attainable. As in Refs. [41], Fig. 3 and [36], Fig. 2d, we can nevertheless compare the $1/d$

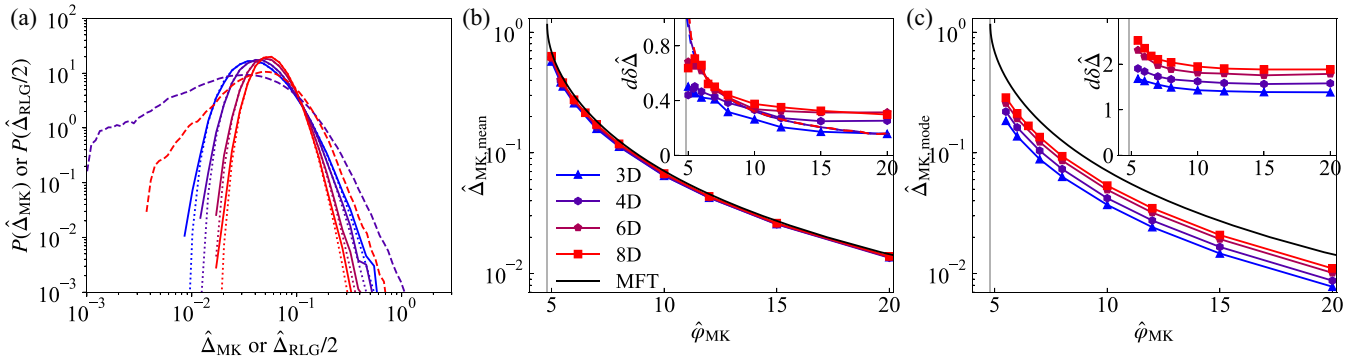

FIG. 2. (a) Distribution of cage sizes for the MK model in $d = 3, 4, 6, 8$ (from blue to red solid line) fit with a log-normal distribution (dotted lines) and compared with the wider distribution obtained in the RLG in $d = 4, 8$ (dashed lines). (b) Mean and (c) modal cage size for the MK model in finite d (points) compared with the $d \to \infty$ MFT predictions (black line) above $\hat{\varphi}_d = 4.81\ldots$ (gray line). Simulation results only slightly undershoot the theoretical curve at all densities. (Inset) Perturbative $1/d$ deviations of the simulation results from the exact $d \to \infty$ MFT predictions. In (b, inset), the Gaussian ansatz estimate for these corrections is included as reference (dashed line), which does not diverge but ends at a finite value beyond the plot range (e.g., 2.5 for $d = 8$).

deviations with those from the Gaussian ansatz. While for the RLG this ansatz was far off the mark [41], for the MK model the results are more nuanced. The prediction significantly underestimates deviations at higher $\hat{\varphi}$, as it does for the RLG, but it describes reasonably well the regime $5.5 \lesssim \hat{\varphi} \lesssim 10$, where a scaling collapse is observed. Because the Gaussian ansatz does not lead to a divergence at $\hat{\varphi}_d$, however, deviations are expected to grow more pronounced as $\hat{\varphi}$ is further decreased toward the dynamical transition. The agreement of the MSD cage in Fig. 2(b) (inset) and [36], Fig. 2(d) should therefore be understood as largely fortuitous. In any event, this overall analysis confirms the perturbative character of the two minimally structured models considered here relative to the exact $d \to \infty$ MFT description.

C. Dynamical fluctuations in the diffusive regime

In order to characterize finite-d deviations from the $d \to \infty$ DMFT results more systematically, we consider the dynamical fluctuations around the theoretical predictions. Different observables for capturing single-particle fluctuations are commonly used, depending on whether the caging or diffusive regime is considered. In the former, one typically considers the scaled four-point susceptibility, i.e., the kurtosis,

$$\left(\frac{\chi_4}{\Delta^2}\right)(t) = \frac{[\langle r^4(t)\rangle]}{[\langle r^2(t)\rangle]^2} - 1, \tag{5}$$

which plateaus at long times. In the latter, because $\chi_4(t)$ diverges at long times we instead consider the non-Gaussian parameter [14],

$$\alpha_2(t) = \frac{d}{d+2}\frac{[\langle r^4(t)\rangle]}{[\langle r^2(t)\rangle]^2} - 1, \tag{6}$$

which vanishes at short and long times and peaks in between. It is well understood that α_2 also vanishes with increasing d [49]. To capture the perturbative behavior of this observable properly, we here instead study the dimensionally rescaled $\hat{\alpha}_2(\hat{t}) = d\alpha_2(\hat{t})$. Note that $\hat{\chi}_4$ and $\hat{\alpha}_2$ are linearly related at constant d [see Ref. [14], Eq. (7)],

$$\hat{\alpha}_2 = \frac{d}{d+2}\left(\frac{\hat{\chi}_4}{\hat{\Delta}^2} - 2\right), \tag{7}$$

which in the limit $d \to \infty$ simplifies to $\hat{\alpha}_2 = \hat{\chi}_4/\hat{\Delta}^2 - 2$. Note also that the full time evolution of $\hat{\chi}_4(\hat{t})$, like that of $\hat{\chi}_4(\hat{t} \to \infty)$, does not simply map between the MK model and RLG, as further discussed in Sec. III D.

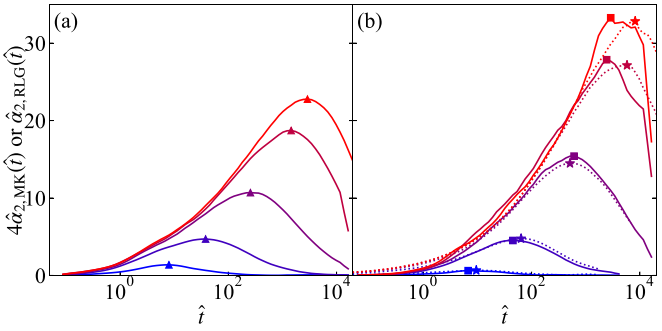

FIG. 3. Time evolution of $\hat{\alpha}_2$ for the largest attained dimension of (a) the MK model in $d = 8$ at $\hat{\varphi} = 1, 3, 4, 4.4, 4.5$ and (b) the RLG with Newtonian (solid line) and Brownian (dotted lines) dynamics in $d = 24$ at corresponding $\hat{\varphi} = 0.5, 1.5, 2, 2.2, 2.25$ (blue to red lines). Note that the percolation transition of the $d = 24$ RLG lies far above the density range considered. In both cases a single peak grows and moves to longer times as $\hat{\varphi} \to \hat{\varphi}_d^-$. Peaks are highlighted with markers.

The time evolution of $\hat{\alpha}_2$ at various $\hat{\varphi} < \hat{\varphi}_d$ is shown in Figs. 3 and 4. The results are qualitatively reminiscent of what has long been reported in supercooled liquids [30–32], and, as expected [50], both Newtonian and Brownian dynamics give rise to fairly similar curves as density increases. Recall that Ref. [14] identified the MFT-like growth of α_2 to be associated with particle displacements along different dimensions to be correlated. The growth of α_2 as $\hat{\varphi}$ increases is therefore here consistent with cage escapes then proceeding through low-dimensional pathways within which motion along many directions is severely constrained, such as transport through tunnel-like openings [14].

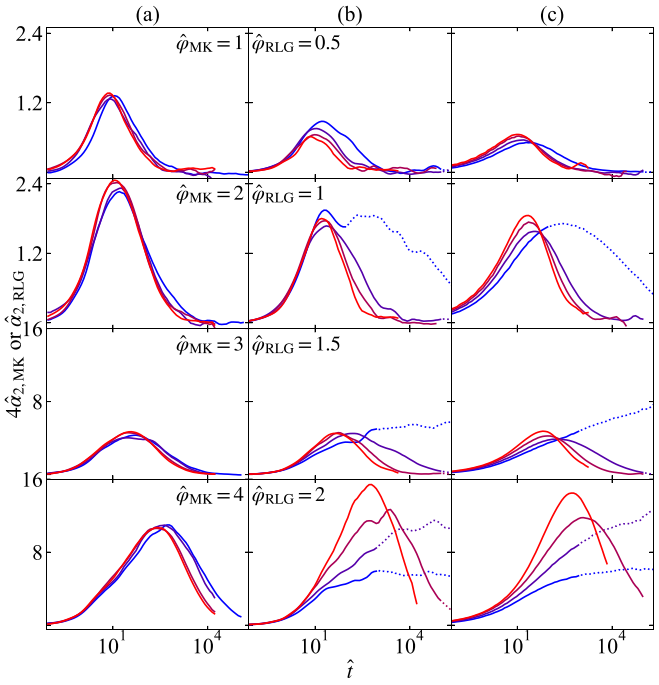

FIG. 4. Evolution of $\hat{\alpha}_2$ for (a) the MK model for $d = 3, 4, 6, 8$ (blue to red lines) at $\hat{\varphi} = 1, 2, 3, 4$ and the RLG with (b) Newtonian and (c) Brownian dynamics for $d = 3, 6, 12, 24$ (blue to red lines) at corresponding $\hat{\varphi} = 0.5, 1, 1.5, 2$. Both systems exhibit a single peak that grows and moves to longer times as $\hat{\varphi} \to \hat{\varphi}_d^-$ (see also Fig. 3). (Note that the ordinate axis uses a different scale in the upper and lower panels.) While $\hat{\alpha}_2$ presents a similar peak compared to the MK model, percolation physics intervenes in the RLG at long times for the larger densities. The resulting deviations are particularly marked at small d (dotted out curves) and result in $\hat{\alpha}_2$ peaking at much longer times.

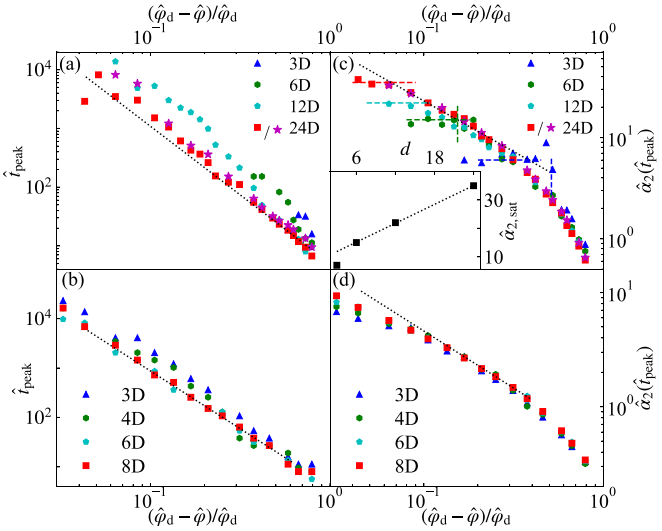

FIG. 5. Peak characteristics for $\hat{\alpha}_2(\hat{t})$. Growth of the peak time for (a) the RLG and (b) the MK model as $\hat{\varphi}$ approaches $\hat{\varphi}_d$ for different d. In both systems the results are roughly consistent with the expected critical scaling $\hat{t}_{peak} \sim (\hat{\varphi}_d - \hat{\varphi})^{-\gamma}$ with $\gamma = 2.34\ldots$ (black dotted line). Evolution of the peak height for (c) the RLG and (d) the MK model as $\hat{\varphi}$ approaches $\hat{\varphi}_d$. The growth first follows the expected critical scaling $\hat{\alpha}_2(\hat{t}_{peak}) \sim (\hat{\varphi}_d - \hat{\varphi})^{-1}$ (black dotted line), but eventually saturates. In (c) results deviate from this trend around the percolation threshold ($\hat{\varphi}_p$ for $d = 3, 6$ are marked as vertical dashed lines). (Inset) The saturation plateau of $\hat{\alpha}_2(\hat{t}_{peak})$ grows roughly linearly with d (dotted line). In (a), (c), Brownian dynamics results for the RLG at $d = 24$ are additionally plotted (purple stars).

Before considering the simulation results in more detail, however, an important caveat must be made. Because α_2 diverges at the *nonperturbative* percolation transition of the RLG [16,51], results for $\hat{\varphi} \gtrsim \hat{\varphi}_p$ must be neglected in order to assess the *perturbative* physics associated with small fluctuations around the exact $d \to \infty$ MFT results.

Once that is done, $\hat{\alpha}_2(\hat{t})$ presents a single peak at nearly the same time for all d and at low densities the full curves collapse reasonably well (Fig. 4). Upon approaching $\hat{\varphi} \to \hat{\varphi}_d$, however, peaks no longer collapse and instead grow with d (see, e.g., Fig. 4, bottom panels). What gives rise to these deviations? Recall that MFT (for $d \to \infty$) finds that this peak should diverge for $\hat{\varphi} \to \hat{\varphi}_d^+$ and that a similar singularity is expected for $\hat{\varphi} \to \hat{\varphi}_d^-$ [14]. In finite d, two phenomena could be at play: (i) activated events turn any MFT divergences into a crossover in finite d [3] and (ii) the number of directions along which particle motion can be correlated is finite, thus bounding the growth of α_2.

Quantifying peak characteristics offers some insight into which phenomenon dominates in this regime. First, consider the peak time. Peak non-Gaussianity coincides with cage escape and is therefore expected to follow the growth of the structural relaxation time. We then expect a scaling $\hat{t}_{peak} \sim (\hat{\varphi}_d - \hat{\varphi})^{-\gamma}$ with a nonuniversal exponent γ, which for $d \to \infty$ is $\gamma = 2.34\ldots$ [52]. Remarkably, over the accessible dynamical range, both models roughly follow that scaling, with agreement improving as d increases [Figs. 5(a) and 5(b)]. Note that finite d deviations of γ relative to the $d \to \infty$ result have the opposite sign as what has been reported for (standard) hard spheres [13], but given the nonuniversality of the exponent and the absence of any theoretical prediction for it, little can be concluded from this difference.

Second, consider the peak height. MFT suggests that [14,53]

$$\hat{\alpha}_2(\hat{t}_{peak}) \sim |\hat{\varphi}_d - \hat{\varphi}|^{-1}. \tag{8}$$

Upon approaching $\hat{\varphi}_d$, both models appear to follow a master curve given by that scaling [Figs. 5(c) and 5(d)]. These pseudocritical scalings are therefore consistent with an (avoided) critical transition at $\hat{\varphi}_d$ in finite d. Unfortunately, the relevant regime is too short to detect systematic deviation of criticality below the predicted (perturbative) upper critical dimension, $d_u = 8$ [53–55], as has been reported for related exponents [56].

Deviations in peak height from the expected pseudocritical scaling are more revealing. For both systems, the effect gradually decrease as d increases. Remarkably, while for the MK model deviations steadily drift up, for the RLG deviations plateau more sharply. The difference likely reflects the complete absence of cooperativity in the latter system, but whether this effect has to do with perturbative or instantonic processes is not immediately obvious. To see more clearly, we leverage the broad d range accessible for the RLG to determine that

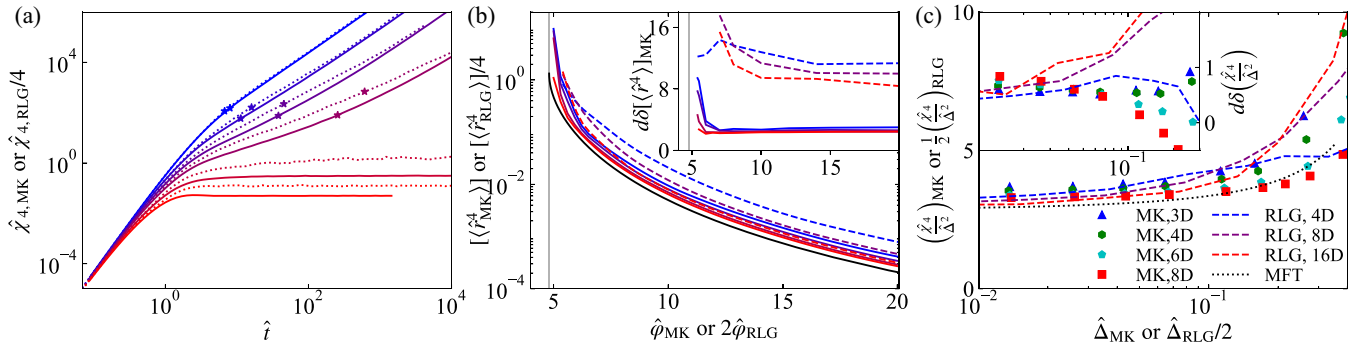

FIG. 6. (a) Time evolution of $\hat{\chi}_4$ for $\hat{\varphi}_{\rm MK} = 2\hat{\varphi}_{\rm RLG} = 1, 2, 3, 4, 6, 8$ (from blue to red lines) for the MK model in $d = 8$ (solid lines) and for the RLG in $d = 24$ (dashed lines). The peak of $\hat{\alpha}_2$ from Fig. 5 (asterisk) occurs at times intermediate between ballistic and diffusive transport. (b) In the caging regime, the mean quartic displacement for the MK model in $d = 3, 4, 6, 8$ (blue to red solid lines) and the RLG in $d = 4, 8, 16$ (blue to red dashed lines) approaches the MFT prediction (black) as d increases. (Inset) Both systems show perturbative $1/d$ corrections, $\delta[\hat{r}^4(\hat{t})] = |([\hat{r}^4_{\rm MFT}(\hat{t})] - [\hat{r}^4(d,\hat{t})])/[\hat{r}^4_{\rm MFT}(\hat{t})]$, but those are markedly larger in the RLG than in the MK model. (c) In the caging regime, long-time $\hat{\chi}_4/\hat{\Delta}^2$ in the MK model (markers) and the RLG (from Ref. [14], dashed lines) converge to the $d \to \infty$ prediction (black dotted line). (Inset) The relative deviation from the MFT prediction in the form of Eq. (11) is consistent with a perturbative correction deep in the caging regime.

the plateau then grows roughly linearly with d [Fig. 5(c) inset]. The peak divergence of α_2 is therefore suppressed as $1/d$, hence suggesting that the plateau height is perturbatively controlled, albeit at a higher order in the expansion than $\hat{\alpha}_2$ more generally.

D. Susceptibility time evolution and long-time scaling

Consistent with the $1/d$ deviations of the MSD from the $d \to \infty$ DMFT differing between the RLG and the MK model (see Fig. 1), $\hat{\alpha}_2$ quantitatively differs between the two systems. This difference cannot be explained by the simple mapping relations given by Eqs. (2) and (7) (Fig. 4). As expressed by Eq. (7), $\hat{\alpha}_2$ depends solely on the MSD and $\hat{\chi}_4$ for a given d. Given that the former is fairly close to the DMFT prediction for both the RLG and the MK model in all d, the main difference in α_2 presented in Sec. III C must therefore come from the latter of the two quantities.

The time evolution of $\hat{\chi}_4$ for the RLG and the MK model is compared in Fig. 6(a) for the highest available d for each system. As expected from Eq. (2), the trivial (factor of 4) mapping collapses the two sets of curves at short times. In the caging regime, the additional multiplicative factor from Eq. (2) separates the two sets of results at long times. In the diffusive regime, Eq. (7) gives that $\hat{\alpha}_2(\hat{t} \to \infty) = 0$ and hence $\hat{\chi}_4 = 2\hat{\Delta}^2$ at long times. Both curves then again converge. At intermediate times, where the non-Gaussian parameter peaks, however, results for the two systems markedly deviate.

To tease out the origin of this difference, we expand the MSD and the mean quartic displacement perturbatively in $1/d$,

$$[\langle \hat{r}^2(\hat{t})\rangle] = \hat{\Delta}_{\rm MFT}(\hat{t}) + A_1(\hat{t})/d + A_2(\hat{t})/d^2 + \cdots,$$
$$[\langle \hat{r}^4(\hat{t})\rangle] = [\langle \hat{r}^4(\hat{t})\rangle]_{\rm MFT} + B_1(\hat{t})/d + B_2(\hat{t})/d^2 + \cdots. \quad (9)$$

Because all d dependencies have been extracted for the $d \to \infty$ MF values in Eq. (9), and hence $[\langle \hat{r}^4\rangle]_{\rm MFT} = \hat{\Delta}^2_{\rm MFT}$, we then have

$$(\hat{\chi}_4/\hat{\Delta}^2)(\hat{t}) = \frac{B_1 - 2A_1\hat{\Delta}_{\rm MFT}}{\hat{\Delta}^2_{\rm MFT}} + O(1/d), \quad (10)$$

where for notational clarity the time dependence is omitted on the right-hand side. Through Eq. (7), $\hat{\alpha}_2(t)$ can then be described *to leading order* by the *leading perturbative* deviation of the MSD from the $d \to \infty$ DMFT results and the mean quartic displacement [see Figs. 1, 2, and 6(b) insets], which are not universal. This correspondence is particularly interesting because it relates fluctuations in finite-d structural glasses to the magnitude of the perturbative $1/d$ deviations from the $d \to \infty$ results. These perturbative effects therefore encode some of the physical features of $d = 3$ systems.

Because quantitative predictions exist for χ_4/Δ^2 in the limit $d \to \infty$, the dimensional convergence of $\hat{\chi}_4$ can also be evaluated. As shown in Fig. 6(c), a solid quantitative agreement is obtained for small cages (i.e., large $\hat{\varphi}$) in both models, with the overall deviations from the $d \to \infty$ scaling as $1/d$ at large $\hat{\varphi}$,

$$\delta\left(\frac{\hat{\chi}_4}{\hat{\Delta}^2}\right) = \left[\left(\frac{\hat{\chi}_4}{\hat{\Delta}^2}\right) - \left(\frac{\hat{\chi}_4}{\hat{\Delta}^2}\right)_{\rm MFT}\right] \Big/ \left(\frac{\hat{\chi}_4}{\hat{\Delta}^2}\right)_{\rm MFT} \sim 1/d. \quad (11)$$

Upon approaching $\hat{\varphi}_{\rm d}$, however, the growth of $\hat{\chi}_4/\hat{\Delta}^2$ deviates from the MFT prediction. For the RLG, it was shown in Ref. [14] that this deviation is due to the presence of weak cages, as captured in the large tail in the distribution of cages around $\hat{\varphi}_{\rm d}$. For the MK model cages are stronger and more narrowly distributed than for the RLG, as discussed above. The results therefore more closely trail the $d \to \infty$ prediction. Results for $d = 8$, however, are somewhat confounding. We suspect that deviations around $\hat{\varphi}_{\rm d}$ might be due to finite-d effects associated with the difference between mean and modal quantities, but identifying the optimal finite-d estimator for χ_4 in this regime is left for future studies.

IV. CONCLUSION

Using state-of-the-art numerical simulations, we have studied the fluctuations of two minimally structured glass formers in finite d, thus identifying the non-Gaussian parameter α_2 as a perturbative $1/d$ deviation from the exact $d \to \infty$ MFT results. The observable is therefore intimately related to mean-field–like (i.e., perturbative) cage escapes [14] and not solely to (nonperturbative) hopping [16,36], as has sometimes been suggested [32]. Given the physical centrality and dimensional robustness of the simulation results for α_2, a description of small fluctuations around the DMFT in the diffusive regime would be a significant enrichment of the theory of simple structural glasses. The numerical results presented in this work can serve both as targets for a future such calculation and, in the meantime, as reference for the study of single-particle fluctuations in (standard) hard sphere glass formers. Such fluctuation-based comparison would offer a much more stringent test of the MFT (and of theories of glasses more generally) for model glass formers than has thus far been possible.

More generally, the overall success of this work motivates further pursuing the program of extracting the out-of-equilibrium DMFT description from finite-d simulations of minimally structured model glass formers. Insight into the mean-field–like features that survive in $d = 3$ system will then be more readily obtained than has thus far been possible by solving the associated equations.

Data relevant to this work have been archived and can be accessed at Duke digital repository [57].

ACKNOWLEDGMENTS

We thank G. Folena, F. Ricci-Tersenghi, A. Manacorda, and F. Zamponi for various stimulating discussions and the latter two also for sharing updated DMFT results for Fig. 8. Computations were carried out on the Duke Compute Cluster. This work was supported by a grant from the Simons Foundation (Grant No. 454937).

APPENDIX A: NONUNIVERSAL MAPPING OF SUSCEPTIBILITY

From Eq. (1), one expects

$$\hat{\chi}_{4,\mathrm{RLG}} \leftrightarrow 4\hat{\chi}_{4,\mathrm{MK}}, \tag{A1}$$

but this expression only holds at short times and in the long-time diffusive limit ($\hat{\varphi} < \hat{\varphi}_\mathrm{d}$), in which cases the tracer displacement is Gaussian by construction. In the long-time caging limit, although Eq. (1) still holds, Eq. (A1) does not. In that regime, $\hat{\chi}_4$ is nonzero as a result of $1/d$ corrections from the $d \to \infty$ result to $[\langle \hat{r}^4(t)\rangle]$ and $\hat{\Delta}$ (as discussed in Sec. III D).

A mapping is nevertheless still possible in the long-time caging limit. Recall that in Ref. [36], Eqs. (S11-13), the MFT estimate of cage size of the MK model was computed from a Gaussian random variable of variance A_MK, which measures the cage size along one direction with $\Delta = 2dA_\mathrm{MK}$. Reference [16] further noted that the large variance term has the form $\hat{\Delta} = (\hat{\Delta}_\mathrm{tracer} + \hat{\Delta}_\mathrm{obstacle})/2$, where for the MK model Δ_tracer and Δ_obstacle are equivalent, whereas in the RLG the obstacles are pinned, i.e., $\Delta_\mathrm{obstacle} = 0$. As a result, Δ_RLG and Δ_MK involve d and $2d$ independent random variables, respectively, and, therefore,

$$\begin{aligned} \Delta_\mathrm{RLG} &= dA_\mathrm{RLG}, \\ \Delta_\mathrm{MK} &= d(A_\mathrm{MK,tracer} + A_\mathrm{MK,obstacle}) = 2dA_\mathrm{MK}. \end{aligned} \tag{A2}$$

Because $\Delta_\mathrm{RLG} \leftrightarrow 2\Delta_\mathrm{MK}$, we have $A_\mathrm{RLG} \leftrightarrow 4A_\mathrm{MK}$, and the contribution of the variance of the cage size due to single random variable is $\mathrm{Var}(A_\mathrm{RLG}) \leftrightarrow 16\mathrm{Var}(A_\mathrm{MK})$. Equation (A2) also gives that the expected variance is

$$\begin{aligned} \mathrm{Var}(\Delta_\mathrm{RLG}) &= d\mathrm{Var}(A_\mathrm{RLG}), \\ \mathrm{Var}(\Delta_\mathrm{MK}) &= 2d\mathrm{Var}(A_\mathrm{MK}). \end{aligned} \tag{A3}$$

We then have $\mathrm{Var}(\Delta_\mathrm{RLG}) \leftrightarrow 8\mathrm{Var}(\Delta_\mathrm{MK})$, i.e.,

$$\hat{\chi}_{4,\mathrm{RLG}} \leftrightarrow 8\hat{\chi}_{4,\mathrm{MK}}. \tag{A4}$$

More physically, the additional factor of 2 relative to Eq. (A1) comes from the different number of independent terms in the variance. In the RLG only the tracer is oscillating within the cage, whereas in the MK model both the tracer and the surrounding obstacles are random variables that contribute to caging.

APPENDIX B: COLLISION RATE SCALING

The collision rate of the RLG tracer can be derived using standard kinetic theory analysis. Suppose a tracer colliding at the origin and moving freely to r. The probability that the tracer has a free run up to r is given by the probability that obstacles are absent within a cylinder with top area of a half unit sphere and length r. This shell has volume $V_\mathrm{shell} = V_{d-1}r$. For Poisson distributed obstacles, the cumulative probability that the first collision happens at range $(0, r)$, $Q_\mathrm{collision}(r)$, then satisfies the relation

$$Q_\mathrm{collision}(r) = 1 - \exp(-\rho V_{d-1} r). \tag{B1}$$

The average free distance available to the tracer is therefore

$$\bar{r} = \int_0^\infty \frac{\mathrm{d}Q_\mathrm{collision}(r)}{\mathrm{d}r} r\,\mathrm{d}r = \frac{1}{\rho V_{d-1}}, \tag{B2}$$

and its collision rate, with the time unit scaled as $\hat{t} = \sqrt{d}t$ is

$$\hat{Z}_\mathrm{tracer} = 1/(\sqrt{d}\bar{r}) = (d\hat{\varphi}/\sqrt{\pi d})\frac{\Gamma\left(1+\frac{d}{2}\right)}{\Gamma\left(\frac{1+d}{2}\right)}. \tag{B3}$$

Recall that $\rho V_d = d\hat{\varphi}$. We then obtain the large d limit scaling of $\hat{Z}_\mathrm{tracer}$ as

$$\hat{Z}_\mathrm{tracer} \sim \frac{d\hat{\varphi}}{\sqrt{2\pi}}. \tag{B4}$$

Figure 7 presents numerical results for $\hat{Z}_\mathrm{tracer}$. The $d, \hat{\varphi}$ scaling and the large d limit are all consistent with Eq. (B4). The $1/d$ correction, however, has the opposite sign as that predicted by Eq. (B3). Correlations between collisions, which are neglected in the above treatment and grow with $\hat{\varphi}$, are likely at the origin of this discrepancy. Calculation of the associated $1/d$ correction, however, is left for future consideration.

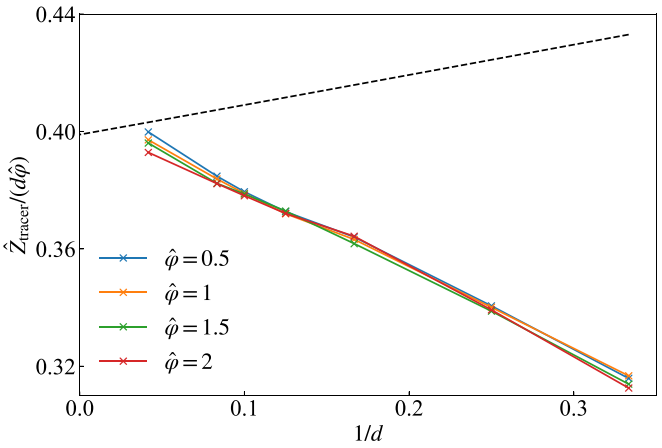

FIG. 7. Scaling of the tracer collision rate $\hat{Z}_{\text{tracer}}$. Crosses are simulation results for various obstacle densities. Black dashed line denotes the relation of Eq. (B3).

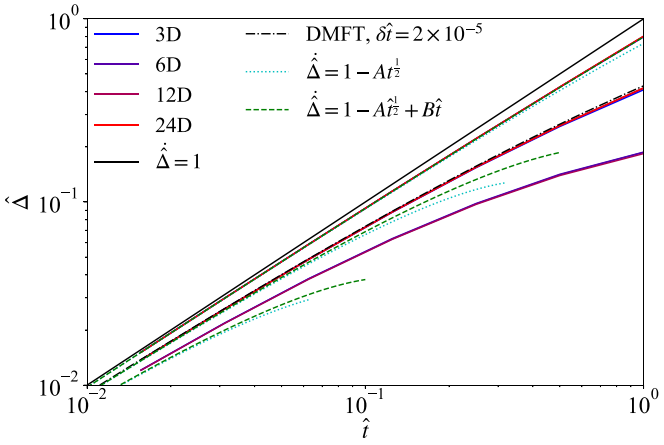

FIG. 8. Brownian dynamics of RLG at short time for $\hat{\varphi}=0.5$, 2, 4 (from top to bottom), compared with the DMFT result of smaller integration step ($\delta t = 2\times10^{-5}$) as well as the expansion forms of Eqs. (C5) and (C6).

APPENDIX C: SHORT-TIME EXPANSION OF DMFT EQUATION FOR BROWNIAN DYNAMICS

For Brownian hard spheres, the DMFT equation (Ref. [19], Eq. (3)) reads

$$\frac{\partial\hat{\Delta}}{\partial\hat{t}} = 1 - \int_0^{\hat{t}} \mathrm{d}u\, \mathcal{M}_{\text{HS}}(\hat{t}-u)\frac{\partial\hat{\Delta}}{\partial u}, \tag{C1}$$

where $\mathcal{M}_{\text{HS}}(t)$ is the memory function. We here seek a short-time analytical expansion form of $\hat{\Delta}(\hat{t})$ from this equation.

Replacing $\mathcal{M}_{\text{HS}}$ with the first-order approximation of $\hat{\varphi}$ (Ref. [19], Eq. (24)),

$$\begin{aligned}\mathcal{M}_{\text{HS}}(\hat{t}) &= \hat{\varphi}\mathcal{M}^{(1)}_{\text{HS}}(\hat{t}) + \mathcal{O}(\hat{\varphi}^2)\\ &= \frac{\hat{\varphi}}{2}\left[\frac{\exp(-\hat{t}/4)}{\sqrt{\pi\hat{t}}} - \frac{\operatorname{erfc}(\sqrt{\hat{t}}/2)}{2}\right] + \mathcal{O}(\hat{\varphi}^2)\\ &= \frac{\hat{\varphi}}{2}\left[\frac{1}{\sqrt{\pi\hat{t}}} - \frac{1}{2} + \mathcal{O}(\hat{t}^{\frac{1}{2}})\right] + \mathcal{O}(\hat{\varphi}^2),\end{aligned} \tag{C2}$$

and assuming

$$\frac{\partial\hat{\Delta}}{\partial\hat{t}} = 1 - A(\hat{\varphi})\hat{t}^{\frac{1}{2}} + B(\hat{\varphi})\hat{t} + \mathcal{O}(t^2), \tag{C3}$$

we can solve for the integral equation (C1) and evaluate the coefficients

$$\begin{aligned}A &= \hat{\varphi}/\sqrt{\pi},\\ B &= \frac{\hat{\varphi}}{4}(1+\hat{\varphi}).\end{aligned} \tag{C4}$$

Note that we only keep linear terms of $\hat{\varphi}$ in A, B because Eq. (C2) is expanded to that order. We then have

$$\hat{\Delta}_{\text{HS}}(t) = \hat{t} - \frac{2}{3}\frac{\hat{\varphi}_{\text{HS}}}{\sqrt{\pi}}\hat{t}^{\frac{3}{2}} + \frac{\hat{\varphi}_{\text{HS}}}{8}\hat{t}^2 + \mathcal{O}(\hat{t}^3). \tag{C5}$$

For the RLG, the mapping gives

$$\hat{\Delta}_{\text{RLG}}(t) = \hat{t} - \frac{2\sqrt{2}}{3}\frac{\hat{\varphi}_{\text{RLG}}}{\sqrt{\pi}}\hat{t}^{\frac{3}{2}} + \frac{\hat{\varphi}_{\text{RLG}}}{8}\hat{t}^2 + \mathcal{O}(\hat{t}^3). \tag{C6}$$

The short-time simulation results are fully consistent with Eq. (C6) (Fig. 8). The expansion results also highlight that noticeable corrections—up to the subdominant correction term ($B\hat{t}$)—become increasingly pronounced at higher densities. The short-time discrepancy in Fig. 7(b) is therefore clearly due to numerical accuracy issues with solving Eq. (C1). In particular, setting a smaller numerical integration step $\delta\hat{t} = 2\times10^{-5}$ (instead of $\delta\hat{t} = 10^{-2}$ in Ref. [19]) results in a much closer agreement with simulation results.

[1] W. Götze, *Complex Dynamics of Glass-Forming Liquids: A Mode-Coupling Theory* (Oxford University Press, Oxford, 2009), Vol. 143.

[2] G. Parisi and F. Zamponi, Mean-field theory of hard sphere glasses and jamming, Rev. Mod. Phys. **82**, 789 (2010).

[3] P. Charbonneau, J. Kurchan, G. Parisi, P. Urbani, and F. Zamponi, Glass and jamming transitions: From exact results to finite-dimensional descriptions, Annu. Rev. Condens. Matter Phys. **8**, 265 (2017).

[4] G. Parisi, P. Urbani, and F. Zamponi, *Theory of Simple Glasses: Exact Solutions in Infinite Dimensions* (Cambridge University Press, Cambridge, UK, 2020), Chap. 4.

[5] A. Seguin and O. Dauchot, Experimental evidence of the gardner phase in a granular glass, Phys. Rev. Lett. **117**, 228001 (2016).

[6] A. P. Hammond and E. I. Corwin, Experimental observation of the marginal glass phase in a colloidal glass, Proc. Natl. Acad. Sci. USA **117**, 5714 (2020).

[7] H. Xiao, A. J. Liu, and D. J. Durian, Probing gardner physics in an active quasithermal pressure-controlled granular system of noncircular particles, Phys. Rev. Lett. **128**, 248001 (2022).

[8] L. Kool, P. Charbonneau, and K. E. Daniels, Gardner-like crossover from variable to persistent force contacts in granular crystals, Phys. Rev. E **106**, 054901 (2022).

[9] A. Ikeda and K. Miyazaki, Mode-coupling theory as a mean-field description of the glass transition, Phys. Rev. Lett. **104**, 255704 (2010).
[10] I. Pihlajamaa, V. E. Debets, C. C. L. Laudicina, and L. Janssen, Unveiling the anatomy of mode-coupling theory, SciPost Phys. **15**, 217 (2023).
[11] C. Liu, G. Biroli, D. R. Reichman, and G. Szamel, Dynamics of liquids in the large-dimensional limit, Phys. Rev. E **104**, 054606 (2021).
[12] M. Mangeat and F. Zamponi, Quantitative approximation schemes for glasses, Phys. Rev. E **93**, 012609 (2016).
[13] P. Charbonneau, Y. Hu, J. Kundu, and P. K. Morse, The dimensional evolution of structure and dynamics in hard sphere liquids, J. Chem. Phys. **156**, 134502 (2022).
[14] G. Biroli, P. Charbonneau, G. Folena, Y. Hu, and F. Zamponi, Local dynamical heterogeneity in simple glass formers, Phys. Rev. Lett. **128**, 175501 (2022).
[15] G. Folena, G. Biroli, P. Charbonneau, Y. Hu, and F. Zamponi, Equilibrium fluctuations in mean-field disordered models, Phys. Rev. E **106**, 024605 (2022).
[16] G. Biroli, P. Charbonneau, E. I. Corwin, Y. Hu, H. Ikeda, G. Szamel, and F. Zamponi, Interplay between percolation and glassiness in the random Lorentz gas, Phys. Rev. E **103**, L030104 (2021).
[17] T. Maimbourg, J. Kurchan, and F. Zamponi, Solution of the dynamics of liquids in the large-dimensional limit, Phys. Rev. Lett. **116**, 015902 (2016).
[18] G. Szamel, Simple theory for the dynamics of mean-field-like models of glass-forming fluids, Phys. Rev. Lett. **119**, 155502 (2017).
[19] A. Manacorda, G. Schehr, and F. Zamponi, Numerical solution of the dynamical mean field theory of infinite-dimensional equilibrium liquids, J. Chem. Phys. **152**, 164506 (2020).
[20] A. Manacorda and F. Zamponi, Gradient descent dynamics and the jamming transition in infinite dimensions, J. Phys. A **55**, 334001 (2022).
[21] E. Agoritsas, G. Biroli, P. Urbani, and F. Zamponi, Out-of-equilibrium dynamical mean-field equations for the perceptron model, J. Phys. A **51**, 085002 (2018).
[22] E. Agoritsas, T. Maimbourg, and F. Zamponi, Out-of-equilibrium dynamical equations of infinite-dimensional particle systems I. the isotropic case, J. Phys. A **52**, 144002 (2019).
[23] E. Agoritsas, T. Maimbourg, and F. Zamponi, Out-of-equilibrium dynamical equations of infinite-dimensional particle systems. II. the anisotropic case under shear strain, J. Phys. A **52**, 334001 (2019).
[24] P. K. Morse, S. Roy, E. Agoritsas, E. Stanifer, E. I. Corwin, and M. L. Manning, A direct link between active matter and sheared granular systems, Proc. Natl. Acad. Sci. USA **118**, e2019909118 (2021).
[25] P. Charbonneau and P. K. Morse, Jamming, relaxation, and memory in a minimally structured glass former, Phys. Rev. E **108**, 054102 (2023).
[26] A. Ikeda and K. Miyazaki, Glass transition of the monodisperse Gaussian core model, Phys. Rev. Lett. **106**, 015701 (2011).
[27] C. Toninelli, M. Wyart, L. Berthier, G. Biroli, and J.-P. Bouchaud, Dynamical susceptibility of glass formers: Contrasting the predictions of theoretical scenarios, Phys. Rev. E **71**, 041505 (2005).
[28] L. Berthier, G. Biroli, J.-P. Bouchaud, L. Cipelletti, and W. van Saarloos, *Dynamical Heterogeneities in Glasses, Colloids, and Granular Media* (Oxford University Press, Oxford, 2011), Vol. 150.
[29] A. Rahman, Correlations in the motion of atoms in liquid argon, Phys. Rev. **136**, A405 (1964).
[30] W. Kob, C. Donati, S. J. Plimpton, P. H. Poole, and S. C. Glotzer, Dynamical heterogeneities in a supercooled Lennard-Jones liquid, Phys. Rev. Lett. **79**, 2827 (1997).
[31] R. Yamamoto and A. Onuki, Heterogeneous diffusion in highly supercooled liquids, Phys. Rev. Lett. **81**, 4915 (1998).
[32] L. Berthier and G. Biroli, Theoretical perspective on the glass transition and amorphous materials, Rev. Mod. Phys. **83**, 587 (2011).
[33] M. Fuchs, W. Götze, and M. R. Mayr, Asymptotic laws for tagged-particle motion in glassy systems, Phys. Rev. E **58**, 3384 (1998).
[34] C. Kaur and S. P. Das, Dynamic heterogeneities in a simple liquid over different time scales, Phys. Rev. Lett. **89**, 085701 (2002).
[35] P. Charbonneau, Y. Hu, L. M. C. Janssen, C. C. L. Laudicina, P. K. Morse, I. Pihlajamaa, and G. Szamel (unpublished).
[36] P. Charbonneau, Y. Jin, G. Parisi, and F. Zamponi, Hopping and the Stokes–Einstein relation breakdown in simple glass formers, Proc. Natl. Acad. Sci. USA **111**, 15025 (2014).
[37] B. Charbonneau, P. Charbonneau, Y. Hu, and Z. Yang, High-dimensional percolation criticality and hints of mean-field-like caging of the random Lorentz gas, Phys. Rev. E **104**, 024137 (2021).
[38] F. Krzakala and L. Zdeborová, Hiding quiet solutions in random constraint satisfaction problems, Phys. Rev. Lett. **102**, 238701 (2009).
[39] R. Mari, F. Krzakala, and J. Kurchan, Jamming versus glass transitions, Phys. Rev. Lett. **103**, 025701 (2009).
[40] R. Mari and J. Kurchan, Dynamical transition of glasses: From exact to approximate, J. Chem. Phys. **135**, 124504 (2011).
[41] G. Biroli, P. Charbonneau, Y. Hu, H. Ikeda, G. Szamel, and F. Zamponi, Mean-field caging in a random Lorentz gas, J. Phys. Chem. B **125**, 6244 (2021).
[42] J. H. Conway and N. J. A. Sloane, Soft decoding techniques for codes and lattices, including the Golay code and the Leech lattice, IEEE Trans. Inf. Theory **32**, 41 (1986).
[43] H. Cohn, A. Kumar, S. Miller, D. Radchenko, and M. Viazovska, The sphere packing problem in dimension 24, Ann. Math. **185**, 1017 (2017).
[44] A. Vardy and Y. Be'ery, Maximum likelihood decoding of the Leech lattice, IEEE Trans. Inf. Theory **39**, 1435 (1993).
[45] A. van Poppelen, Cryptographic decoding of the Leech lattice, Master's thesis, Utrecht University, 2016.
[46] M. Skoge, A. Donev, F. H. Stillinger, and S. Torquato, Packing hyperspheres in high-dimensional Euclidean spaces, Phys. Rev. E **74**, 041127 (2006).
[47] G. Foffi, C. De Michele, F. Sciortino, and P. Tartaglia, Scaling of dynamics with the range of interaction in short-range attractive colloids, Phys. Rev. Lett. **94**, 078301 (2005).
[48] A. Scala, T. Voigtmann, and C. De Michele, Event-driven brownian dynamics for hard spheres, J. Chem. Phys. **126**, 134109 (2007).
[49] M. Adhikari, S. Karmakar, and S. Sastry, Spatial dimensionality dependence of heterogeneity, breakdown of the Stokes–Einstein

relation, and fragility of a model glass-forming liquid, J. Phys. Chem. B **125**, 10232 (2021).

[50] T. Gleim, W. Kob, and K. Binder, How does the relaxation of a supercooled liquid depend on its microscopic dynamics? Phys. Rev. Lett. **81**, 4404 (1998).

[51] F. Höfling, T. Munk, E. Frey, and T. Franosch, Critical dynamics of ballistic and brownian particles in a heterogeneous environment, J. Chem. Phys. **128**, 164517 (2008).

[52] J. Kurchan, G. Parisi, P. Urbani, and F. Zamponi, Exact theory of dense amorphous hard spheres in high dimension. II. the high density regime and the gardner transition, J. Phys. Chem. B **117**, 12979 (2013).

[53] S. Franz, G. Parisi, F. Ricci-Tersenghi, and T. Rizzo, Field theory of fluctuations in glasses, Eur. Phys. J. E **34**, 102 (2011).

[54] G. Biroli and J.-P. Bouchaud, Critical fluctuations and breakdown of the Stokes-Einstein relation in the mode-coupling theory of glasses, J. Phys.: Condens. Matter **19**, 205101 (2007).

[55] S. Franz, H. Jacquin, G. Parisi, P. Urbani, and F. Zamponi, Quantitative field theory of the glass transition, Proc. Natl. Acad. Sci. USA **109**, 18725 (2012).

[56] L. Berthier, P. Charbonneau, and J. Kundu, Finite dimensional vestige of spinodal criticality above the dynamical glass transition, Phys. Rev. Lett. **125**, 108001 (2020).

[57] https://doi.org/10.7924/r4tt4tq52.